




Cell atlas of the human ocular anterior segment: Tissue-specific and shared cell types

Tavé van Zyl^{a,b,c,1,2,3}, Wenjun Yan^{b,c,1}, Alexi M. McAdams^{a,b,c,4}, Aboozar Monavarfeshani^{b,c,d}, Gregory S. Hageman^{e,f} , and Joshua R. Sanes^{b,c,2} 

Contributed by Joshua R. Sanes; received January 18, 2022; accepted May 26, 2022; reviewed by Steven Bassnett, Robert Lavker, and Joel Schuman

The anterior segment of the eye consists of the cornea, iris, ciliary body, crystalline lens, and aqueous humor outflow pathways. Together, these tissues are essential for the proper functioning of the eye. Disorders of vision have been ascribed to defects in all of them; some disorders, including glaucoma and cataract, are among the most prevalent causes of blindness in the world. To characterize the cell types that compose these tissues, we generated an anterior segment cell atlas of the human eye using high-throughput single-nucleus RNA sequencing (snRNAseq). We profiled 195,248 nuclei from nondiseased anterior segment tissues of six human donors, identifying >60 cell types. Many of these cell types were discrete, whereas others, especially in the lens and cornea, formed continua corresponding to known developmental transitions that persist in adulthood. Having profiled each tissue separately, we performed an integrated analysis of the entire anterior segment, revealing that some cell types are unique to a single structure, whereas others are shared across tissues. The integrated cell atlas was then used to investigate cell type-specific expression patterns of more than 900 human ocular disease genes identified through either Mendelian inheritance patterns or genome-wide association studies.

cornea | lens | iris | trabecular meshwork | ciliary body

The anterior segment of the eye is a complex set of interconnected structures, comprising the cornea, conjunctiva, iris, ciliary body (CB), crystalline lens, and aqueous humor outflow pathways; the outflow pathways, in turn, include the trabecular meshwork (TM), Schlemm canal, and ciliary muscle (Fig. 1 *A* and *B*). Together, these structures fulfill two prerequisites of vision: 1) ensuring that light reaches the retina and 2) ensuring that it is optimally focused. The transparent cornea and lens provide the refractive power of the eye. The iris determines how much light reaches the retina. The CB produces the aqueous humor that nourishes the cornea and lens and removes waste products. Finally, the outflow pathways drain aqueous humor from the anterior chamber.

Because each of the structures within the anterior segment is essential for proper functioning of the eye, dysfunction of any one of them leads to vision loss. Indeed, the three leading causes of global blindness among adults ages >50 y involve anterior segment structures to varying extents: cataract, glaucoma, and uncorrected refractive error (1). Other conditions with manifestations primarily in the anterior segment include dry eye disease, corneal dystrophies, anterior uveitis and trachoma. Although most of these entities can be treated, few if any can be cured with current approaches.

To build a better understanding of the complex tissues comprising the human anterior segment, we generated a cell atlas using high-throughput single-nucleus RNA sequencing (snRNAseq). We profiled 195,248 single nuclei from six nondiseased anterior segment tissues, applied computational methods to cluster them based on transcriptomic similarity, and used histological techniques to assign cell type identities to the clusters. After investigating each tissue independently, we pooled them and performed an integrated analysis. In this way, we were able to show that some cell types are confined to specific tissues, whereas others are shared across tissues. Finally, we used this cell atlas to investigate cell-type-specific expression patterns of over 900 genes that have been implicated in susceptibility to human ocular diseases.

Results

Six tissues—central cornea, corneoscleral wedge (CSW), TM, iris, CB, and lens—were dissected from eyes of six individual donors with no histories of ocular disease (*SI Appendix, Table S1*). Tissues were obtained postmortem within <6 h from death in all but one case, dissected within an hour of enucleation, and frozen for further processing. Nuclei were prepared and profiled using a droplet-based method (2). Altogether, we obtained high-quality transcriptomes from 195,248 single nuclei from which we

Significance

Several of the most prevalent blinding ocular conditions worldwide, including glaucoma, cataract, and uncorrected refractive error, involve structures of the anterior segment of the human eye, which consists of the cornea, iris, ciliary body, crystalline lens, and aqueous humor outflow pathways. In addition to providing transcriptomic profiles of the cell types within individual tissues, this work contributes to our understanding of the relatedness and diversity of these cell types across contiguous tissues by generating an integrated anterior segment cell atlas and documenting the expression of more than 900 disease-associated genes in each cell type. By allowing simultaneous interrogation of cell type-specific expression of genes across multiple tissues, the atlas may yield broad insight into normal and disease-associated anterior segment functions.

Competing interest statement: T.v.Z. is employed by Regeneron. J.R.S. is a consultant to Biogen. This work was performed entirely at Harvard University, with no funding from either Regeneron or Biogen. Regeneron and Biogen scientists have had no access to the data.

Copyright © 2022 the Author(s). Published by PNAS. This article is distributed under [Creative Commons Attribution-NonCommercial-NoDerivatives License 4.0 \(CC BY-NC-ND\)](https://creativecommons.org/licenses/by-nc-nd/4.0/).

¹T.v.Z. and W.Y. contributed equally to this work.

²To whom correspondence may be addressed. Email: tave.vanzyl@yale.edu or sanesj@mcb.harvard.edu.

³Present address: Department of Ophthalmology and Visual Science, Yale School of Medicine, New Haven, CT 06510.

⁴Present address: Division of Chemistry and Chemical Engineering, California Institute of Technology, Pasadena, CA 91125.

This article contains supporting information online at <http://www.pnas.org/lookup/suppl/doi:10.1073/pnas.2200914119/-DCSupplemental>.

Published July 15, 2022.

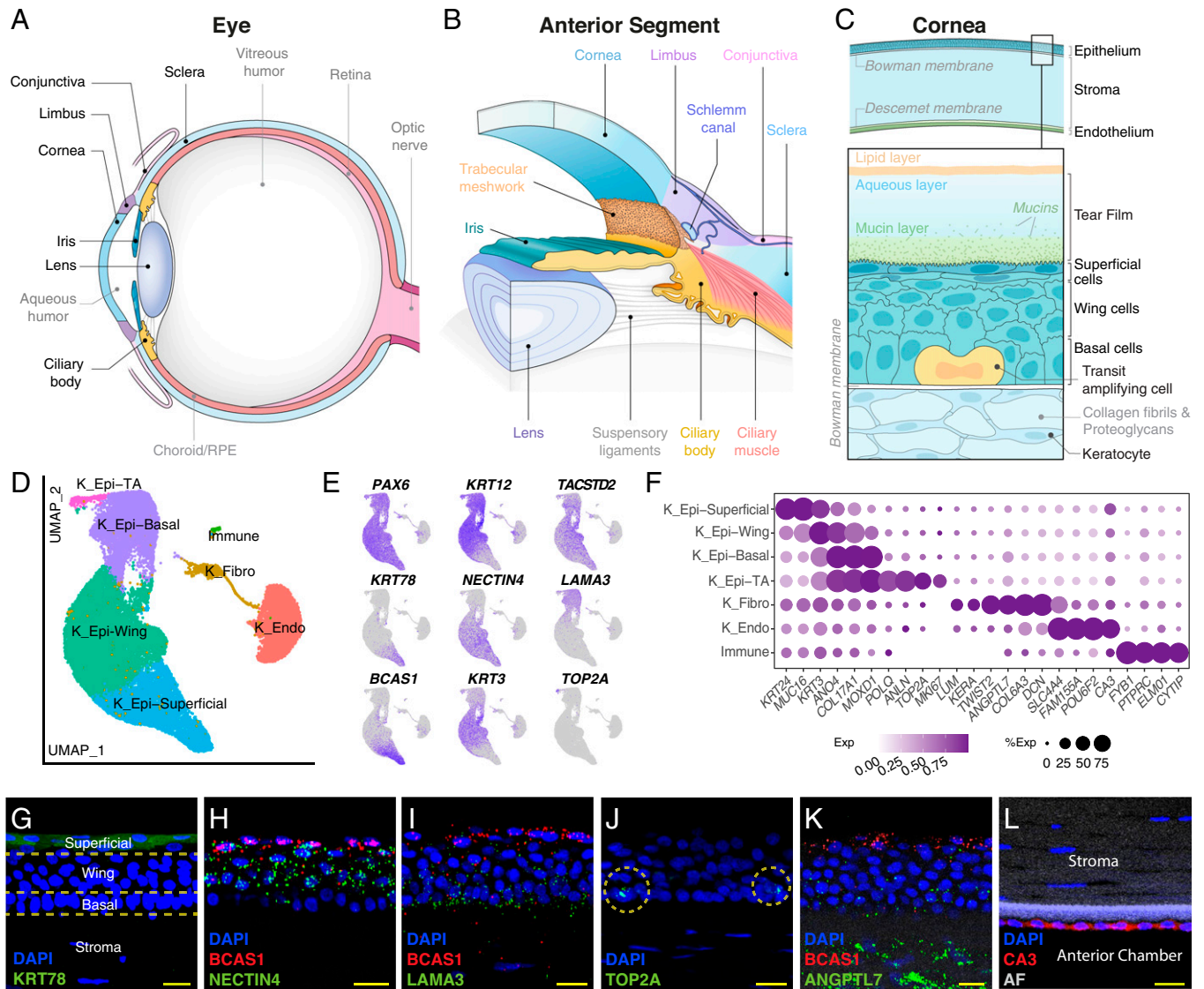


Fig. 1. Human anterior segment and cells of the central cornea. (A) The human eye depicted in sagittal section. (B) The anterior segment, which includes the cornea, iris, CB, and lens. The limbus, representing the transition between peripheral cornea and sclera, houses the aqueous outflow structures including the TM and Schlemm canal. (C) Central cornea comprises three primary cellular layers: epithelium, stroma, and endothelium. The stratified epithelium is composed of basal, wing, and superficial cells delineated in the boxed area. (D) Clustering of 37,485 single-nucleus expression profiles from human central cornea visualized by uniform manifold approximation and projection (UMAP). Here and in subsequent UMAPs, arbitrary colors are used to distinguish clusters deemed to be distinct by unsupervised analysis. (E) Feature plots demonstrating DE genes corresponding to the epithelial subtypes. (F) Dot plot showing genes selectively expressed in cells of the central cornea, with gradient expression patterns noted in the epithelial subtypes. In this and subsequent figures, the size of each circle is proportional to the percentage of nuclei within a cluster expressing the gene and the color intensity depicts the average normalized transcript count in expressing cells. (G) Corneal superficial epithelium immunostained for KRT78 (green). (H) Fluorescent RNA ISH for *BCAS1* (red) highlights superficial epithelium, and *NECTIN4* (green) highlights both wing cells and superficial cells. (I) ISH for *BCAS1* (red) highlights superficial epithelium and *LAMA3* (green) highlights basal cells. (J) Transit amplifying cells are identified via ISH for *TOP2A* (green). (K) Corneal stromal fibroblasts are highlighted by ISH for *ANGPTL7* (green); the superficial epithelium is highlighted by ISH for *BCAS1* (red). (L) Corneal endothelium immunostained for CA3 (red). AF, autofluorescence; K_Epi, corneal epithelium; TA, transit amplifying; K_Fibro, corneal fibroblasts; K_Endo, corneal endothelium. Yellow bars: 20 μ m.

generated a cell atlas. An additional eight eyes were used for histological analysis (*SI Appendix*, Table S2).

Cornea. The transparent, avascular cornea forms a tough layer that, along with the sclera, encases the delicate intraocular tissues. Beyond its protective function, the cornea provides the principal refracting surface of the eye (3). The cornea is composed of 3 primary cellular layers: epithelium, stroma, and endothelium (Fig. 1C). The corneal epithelium is a nonkeratinizing stratified squamous epithelium. Its cells can be divided into three histologically distinct sublayers: an innermost single layer of columnar basal cells, a two- to three-cell-thick intermediate layer of “wing” or polygonal suprabasal cells, and a two-cell-thick superficial layer of plate-like squamous cells. The

basal cell layer contains two cell types: some divide continuously (transit amplifying cells) whereas others arrest and subsequently migrate superficially to become wing and then surface cells. The avascular and acellular Bowman layer separates the epithelium from the lamellar stroma; and the Descemet membrane, a basement membrane, separates the lamellar stroma from the endothelium.

We isolated the central 6 mm of the cornea and processed it separately from the peripheral cornea and limbus, discussed below. We recovered transcriptomes from 37,485 single nuclei and divided them into 7 clusters using computational analysis (*Materials and Methods*). Using established markers, we annotated them as corneal epithelial cells (four clusters, 81.3%), corneal endothelial cells (14.5%), stromal keratocytes (also

known as corneal fibroblasts, 3.6%), and immune cells (0.5%) (Fig. 1 D–F and *SI Appendix*, Fig. S1A, and Dataset S1).

Among corneal epithelial clusters, defined by a high expression of *PAX6*, *KRT12*, and *TACSTD2* (Fig. 1E), we localized differentially expressed (DE) genes by immunohistochemistry and in situ hybridization (ISH) in order to assign each cluster to cells populating distinct sublayers. The basal cluster was characterized by an enriched expression of extracellular matrix (ECM)- and adhesion-related genes including *LAMA3* (Fig. 1E and J). The transit amplifying cells were distinguished from committed basal cells by selective expression of the cell proliferation marker *MKI67* and other genes involved in DNA replication and cell division including *BIRC5*, *UBE2C*, and *TOP2A* (4–8) (Fig. 1E and J). The superficial-most squamous epithelial cells were characterized by the expression of multiple keratins (*KRT4*, *KRT24*, *KRT78*) and mucins (*MUC4*, *MUC16*, *MUC21*, *MUC22*), as well as *BCAS1* (Fig. 1E, H, I, and K and *SI Appendix*, Fig. S2B). The middle layer wing cells were characterized by higher levels of *KRT3* expression and graded expression of multiple genes, representing the transitional state between basal and superficial cells (Fig. 1E, F, and H and *SI Appendix*, Fig. S2A).

Two other clusters corresponded to the corneal endothelium (*CA3*; Fig. 1F and L) and corneal stromal keratocytes (*ANGPTL7*; Fig. 1F and K). Finally, the small cluster of immune cells contained both macrophages (likely corneal dendritic cells) and lymphocytes; DE genes within the cluster included *PTPRC/CD45*, *CYTIP*, *FYB1*, *ELMO*, and lymphocyte-associated marker *IKZF1* (Fig. 1F). The somata of neurons that innervate the cornea are located proximal to the tissue itself, so we did not identify any in our dataset.

Limbus. The limbus is the annular region between the avascular clear cornea and the vascularized opaque sclera (Fig. 2A). The limbus is not anatomically discrete but contains components distinct from both cornea and sclera (9). Externally, it contains the transition zone of the ocular surface where corneal and conjunctival epithelia meet. Herein, limbal epithelial stem cells (LSCs), accounting for less than 1 to 2% of proliferating basal epithelial cells, help maintain corneal epithelial integrity, which keeps the cornea avascular and transparent (10–12). Internally, the limbus includes the TM, Schlemm canal, and specialized outflow vessels through which aqueous humor drains from the anterior chamber.

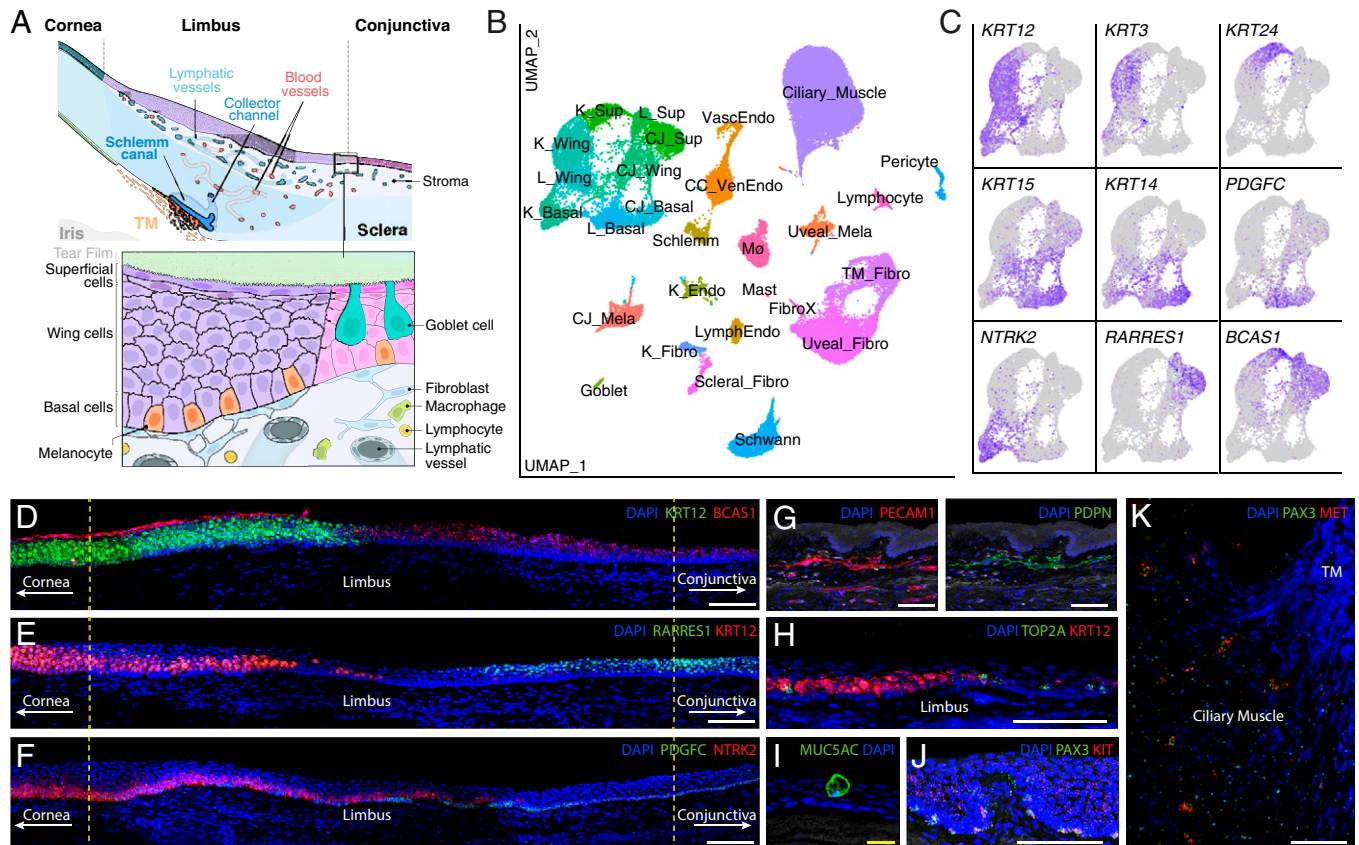


Fig. 2. Cell types of the internal and external limbus derived from dissection of CSW. (A) Diagram of the limbus, representing the transitional tissue between peripheral corneal and sclera. (B) Clustering of 52,309 single-nucleus expression profiles derived from CSW tissue visualized by UMAP. (C) Feature plots showing a selection of genes enriched in ocular surface epithelium subtypes. (D) ISH for *BCAS1* (red) highlights the superficial epithelium in both the cornea and conjunctiva, whereas *KRT12* (green) highlights basal and wing cells of the cornea. A transitional area is noted in the limbus where *KRT12* expression tapers off and is absent in the conjunctival epithelium. Here, and in F, G, and I, the images represent a cropped version of a larger montage obtained from a continuous meridional section spanning cornea, limbus, and sclera, providing anatomical landmarks to support labeling. For an example of the full image, see *SI Appendix*, Fig. S3F. (E) ISH for *KRT12* (green) highlights basal and wing cells of the cornea, and *RARRES1* (green) highlights superficial and some wing cells of the conjunctiva. A transition area within the limbus is noted. (F) ISH for *NTRK2* (red) highlights the basal epithelium of the cornea, and *PDGFC* (green) highlights the basal epithelium of the conjunctiva. (G) Immunostaining against PECAM1 (red) highlights endothelial cells lining vessels in the subepithelial stromal tissues of the external limbus. Immunostaining against PDPN (green) highlights lymphatic endothelium lining a subset of these vessels. (H) Transit amplifying basal cells within the limbus are highlighted with ISH for *TOP2A* (green); basal and wing cells in the limbal area demonstrate *KRT12* (red) expression as visualized by ISH. (I) A goblet cell in the conjunctiva visualized with immunostaining against MUC5AC (green). (J) Conjunctival melanocytes visualized by ISH for *PAX3* (green) and *KIT* (red). (K) Uveal melanocytes visualized by ISH for *PAX3* (green) and *MET* (red). Mø, macrophage; Conj, conjunctival; CC_VenEndo, Collector Channel/Venous Endothelium; Vasc, vascular; Endo, endothelium, K, cornea; Fibro, fibroblast. (Scale bars: 100 μm.)

To ensure adequate representation of cell types in both the internal and external limbus, we separated the TM from the CSW, processed each separately, and merged the data into a single dataset of 52,309 transcriptomes (Fig. 2 *B* and *C* and *SI Appendix*, Figs. *S1B* and *S4 A* and *D*, and *Dataset S1*). Of these, 11,108 were identified as ocular surface epithelial cells based on expression of canonical epithelial markers *CDH1*, *CLDN1*, and keratin genes; we reclustered this group to identify rare types and ensure optimal capture of gradient differences (*SI Appendix*, Figs. *S1C* and *S3A*). This clustering result was then incorporated into the limbus dataset (*Dataset S1*).

Ocular surface epithelium. We identified nine groups of ocular surface epithelial cells, which could be divided into corneal, limbal, and conjunctival populations based on established markers and histological validation (Fig. 2*B* and *SI Appendix*, Fig. *S3A*). Those with robust *KRT12*, *KRT3*, and/or *KRT24* expression were corneal, whereas those with *KRT15*, *KRT14*, *KRT13*, and/or *KRT7* expression were conjunctival or limbal (Fig. 2*C* and *SI Appendix*, Fig. *S4D*) (13–15). The three corneal clusters corresponded to the superficial, wing, and basal types described above (Fig. 1*D*). The three conjunctival clusters were all positive for *IGFBP3*, previously shown to be specific to conjunctival epithelium; among them, we identified basal (e.g., *KRT14+ PDGFC+*), superficial (e.g., *KRT7+ LCN2+ WFDC2+ ENTPD2+*), and wing clusters (e.g., *KRT13+ KRT15+ BCAS1+ RARRES1+*) (*SI Appendix*, Fig. *S3 B* and *C*) (16, 17). The three limbal clusters demonstrated expression profiles reflective of their transitional location; interestingly, limbal superficial and basal cells were transcriptionally more similar to their conjunctival counterparts whereas the limbal wing cells were more transcriptionally similar to their corneal counterparts. Superficial limbal epithelial cells were distinguished and confirmed histologically as *WFDC2-ENTPD1+ BCAS1+ RARRES1+* (*SI Appendix*, Fig. *S3H*). Limbal basal cells were *KRT15+ KRT12- GJB6-*, whereas limbal wing cells were *KRT15+ KRT12+ GJB6+*, consistent with prior reports (18, 19). We visualized the expression patterns of the limbal and conjunctival cells with *ISH* for *KRT12*, *PDGFC*, *WFDC2*, *ENTPD1*, *RARRES1*, and *BCAS1* (Fig. 2 *D–F* and *SI Appendix*, Fig. *S3H*).

Together, the nine clusters related to each other through expression similarities and differences along two orthogonal axes: the corneal–limbal–conjunctival axis, as described above, and the superficial–wing–basal axis. For example, superficial cells of all three regions expressed *KRT4* and *BCAS1*, superficial and wing cells of all three regions expressed *NECTIN4*, and basal cells of all three regions expressed *LAMA3* (*SI Appendix*, Fig. *S3B*). Regarding differences, *MUC16* was the predominant mucin expressed by superficial corneal cells, whereas *MUC4* was the predominant mucin expressed by the limbal and conjunctival counterparts. Similarly, corneal basal epithelial cells were strongly *NTRK2* positive, whereas those in the conjunctiva were *NTRK2* negative but *PDGFC* and *LGR6* positive (Fig. 2 *C* and *F* and *SI Appendix*, Fig. *S3F*). *BCAS1* expression was limited to the superficial epithelial layer in the cornea but present in both the superficial and wing epithelial cells of the conjunctiva (Fig. 2*D*). These layers of the conjunctiva were also positive for *RARRES1* and *MECOM*, unlike their counterparts in the cornea (Fig. 2*E* and *SI Appendix*, Fig. *S3F*).

Three epithelial cell populations that have been reported to be present in this region did not form discrete clusters, namely, transit amplifying cells, limbal progenitor cells (LPCs), and LSCs. The first of these, the transit amplifying cell, was observed in the cornea, as described above, but did not form a distinct cluster in this smaller dataset (3,696 basal epithelia in CSW

sample compared to 8,614 in central cornea; Fig. 2*H* and *SI Appendix*, Fig. *S3D*). Second, although recent reports described separate clusters of LPCs (19–22), we found that certain markers identified in those studies (e.g., *GPHA2*, *CDH19*, and *FRZB*) were expressed by cells in a discrete lobe within the limbal basal cluster (*SI Appendix*, Fig. *S3E*). Other putative LPC/LSC markers were generally enriched in both our limbal and conjunctival basal populations or were more diffusely expressed or undetectable (*SI Appendix*, Fig. *S3G*, and *Dataset S1*). Finally, one study reported a discrete LSC cluster (21), but we find striking transcriptomic similarities between that type and the cells we identify as vascular endothelial cells here and in a previous report (23). We therefore hesitate to nominate LPCs or LSCs here as discrete, recognizable types.

Goblet cells. A distinct cluster corresponding to the specialized, mucin-producing goblet cells of the ocular surface was identified based on enrichment of *MUC5AC* (24) (Fig. 2*I*). This cluster was visualized within the conjunctival epithelium and also expressed *ATP2C2*, *AGR3*, and *TFF1*.

Melanocytes. Two distinct clusters were composed of melanocytes. They shared canonical melanocyte markers, such as *PAX3*, *TYR*, and *MITF*, but were transcriptionally distinct (Fig. 2*C* and *SI Appendix*, Fig. *S4 C* and *D*). Histology supported the presence of two distinct cell types, which we annotate as uveal and conjunctival, corresponding to their locations (Fig. 2 *J* and *K*). The uveal type, derived from both the TM and CSW, represented melanocytes in the ciliary muscle and selectively expressed *ERBB4*, *NRG3*, and *MET*; the conjunctival type, derived exclusively from the CSW, represented melanocytes nestled among the basal epithelial cells of the conjunctiva and selectively expressed *LEF1*, *PLPPR4*, and *KIT*.

Trabecular meshwork. Two clusters of closely related cells demonstrated DE genes previously identified via scRNAseq analysis of TM tissue (23, 25). *ISH* confirmed the localization of these genes to the aqueous drainage structures within the iridocorneal angle, with some clearly confined to the TM and others extending into contiguous tissues of the iris root and ciliary muscle (*SI Appendix*, Fig. *S4 E–G*). The two clusters were tentatively annotated as TM fibroblasts and uveal fibroblasts, with the latter characterized by genes most strongly visualized at the uveal base of the TM, the iris root, and ciliary muscle. Although TM cells are known to have characteristics of vascular endothelia, smooth muscle, and macrophages as well as fibroblasts, we assigned fibroblast as the predominant descriptor due to their transcriptomic relatedness to other fibroblasts in the dataset (e.g., those in the sclera and cornea) (*SI Appendix*, Fig. *S4F*) (26, 27). This does not contradict their hybrid nature, and indeed, we note DE genes in these clusters reminiscent of the above types. For example, *MYOC*, *CEMIP*, *CDH23*, *SLC4A10*, *FAM155A*, *KCNIP1*, *PDE1C*, *ADAM12*, *MICAL2*, and *LMX1B* were among the top 20 DE genes for the TM cluster, whereas *BMP5*, *EYA1*, *BICC1*, *DCN*, *APOD*, *KCNT2*, *ABCA8*, *IGFBP5*, *DYNCL11*, and *MGP* were for the uveal cluster (*Dataset S1*). Gradient expression patterns were noted within and across both clusters (*SI Appendix*, Fig. *S4H*), potentially representing further specialization as described in *Integrated Analysis*.

Vessel endothelium. Transcriptomic profiles identified four clusters of vessel endothelial cells. Based on our previous work (23), we identified one as Schlemm canal endothelium expressing *FNI* and *PLAT* and a second as vascular endothelium, expressing *ALPL* (*SI Appendix*, Fig. *S4D*). A third corresponded to endothelium lining the collector channels, aqueous veins, and scleral venous plexuses, expressing *ACKR1/DARC*, *AQP1*, *SELE*, and *COL15A1*. The fourth endothelial cluster selectively

expressed lymphatic markers including *LYVE1*, *PROX1*, *CCL21*, and *FLT4* and was localized to subepithelial vessels within the conjunctival stroma using immunostaining against PDPN (Fig. 2G). We assigned these cells to the conjunctival lymphatic endothelium.

Additional cell types. Seven additional clusters were identified as pericytes (*NOTCH3* and *PDGFRB*), macrophages (*LYVE1+CD163+*), lymphocytes (*CD69+*), mast cells (*IL1RL1+CPA3+*), ciliary muscle cells (*DES* and *CHRM3*), Schwann cells (*LGI4* and *CDH19*), corneal stromal fibroblasts (*KERA* and *MME*), and scleral fibroblasts (*TXNB*, *FBLN1*). An eighth cluster, provisionally labeled FibroX, was transcriptomically similar to scleral fibroblasts but exhibited distinct markers such as *EBF2* and *SHISA6* (SI Appendix, Fig. S4D).

Iris. The iris functions as a diaphragm akin to those in manufactured optical systems. The iris can be divided into five principal

parts: 1) the anterior border layer, consisting of a dense meshwork of fibroblasts and melanocytes; 2) the stroma, made up of loose connective tissue and a lower density of fibroblasts and melanocytes, along with blood vessels, axons surrounded by Schwann cells, and immune cells such as macrophages (“clump cells”), mast cells, and lymphocytes; (3) the sphincter muscle, made up of spindle-shaped (mononucleated) smooth muscle cells bundled into units of 5 to 8; 4) the dilator muscle, a group of pigmented myoepithelial cells sometimes called anterior pigmented epithelium (APE); and 5) the posterior pigmented epithelium (PPE) facing the posterior chamber (Fig. 3A).

From iris samples, we obtained 57,422 nuclei that formed 9 clusters (Fig. 3B and C and SI Appendix, Fig. S1D). We were able to assign all 9 to cell types. Iris stromal fibroblasts, expressing *DCN*, *APOD*, *MYOC*, *RARRES1*, and *PDPN*, were identified in the stroma and anterior border layer of the iris via immunostaining against PDPN (Fig. 3F). The melanocytes

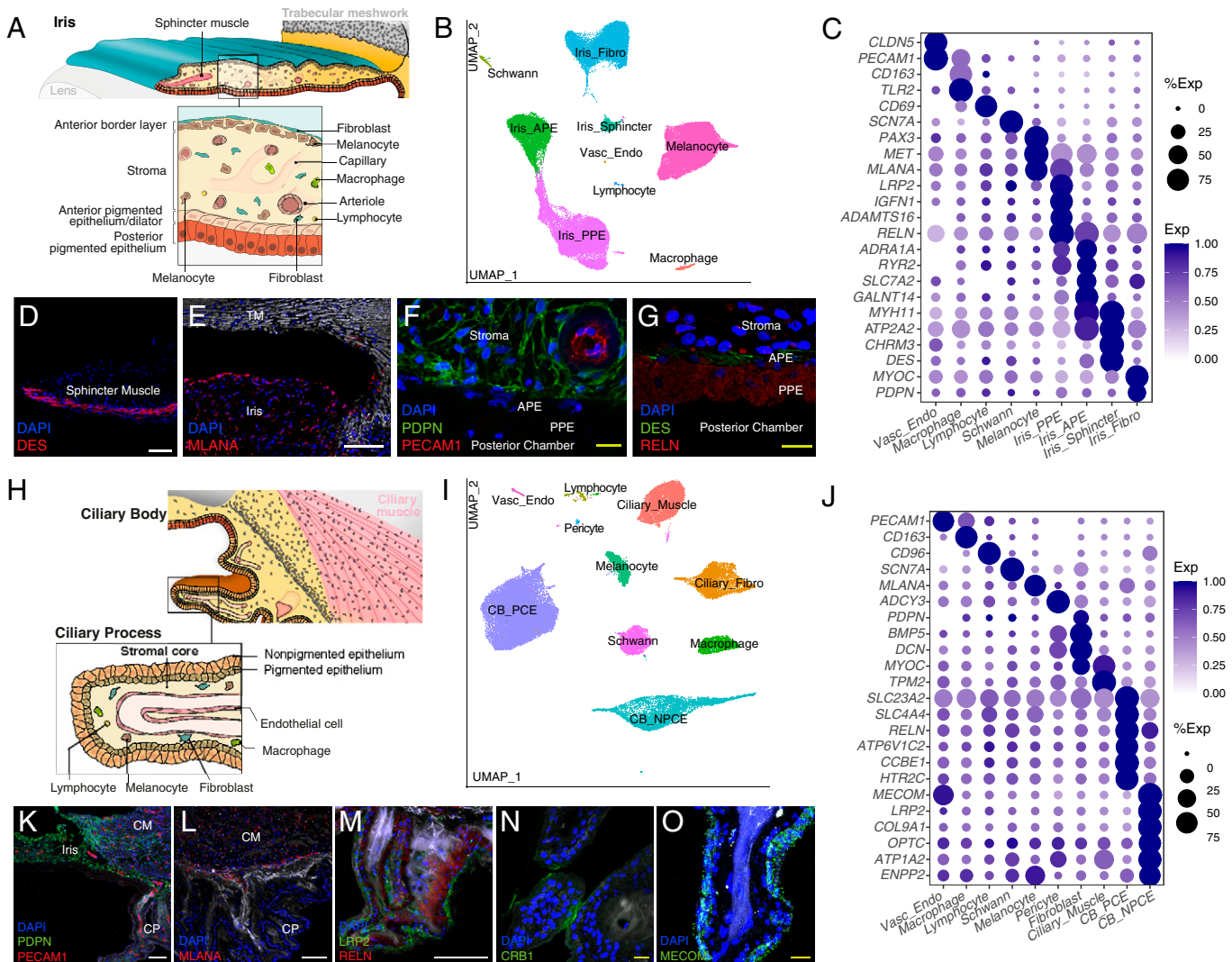


Fig. 3. Cells of the iris and CB. (A) Diagram of the human iris, consisting of the anterior border layer, the stroma, the sphincter muscle, APE, and PPE, shown in greater detail within the box. (B) Clustering of transcriptomes derived from iris tissue visualized by UMAP. (C) Dot plot showing genes selectively expressed in cells of the iris. (D) Iris sphincter muscle cells immunostained for desmin (DES; red). (E) Uveal melanocytes within the anterior border layer and stroma of the iris immunostained for Melan-A (MLANA; red). (F) Iris fibroblasts and vessel endothelium within the iris stroma immunostained with PDPN (green) and PECAM1 (red), respectively. (G) Immunostaining against RELN (red) highlights the iris PPE and to a lesser extent iris APE; the latter is also positive for DES (green), highlighting its contractile role as the iris dilator. (H) Diagram of the human CB, consisting of the ciliary muscle, ciliary stroma, and ciliary processes, shown in greater detail within the box. (I) Clustering of 34,132 single-nucleus expression profiles derived from CB tissue visualized by UMAP. (J) Dot plot showing genes selectively expressed in cells of the CB. (K) Ciliary stromal fibroblasts immunostained with PDPN (green) and vessel endothelium with PECAM1 (red). (L) Uveal melanocytes within the ciliary stroma immunostained for MLANA (red). (M) CB-NPCE and CB-PCE immunostained with LRP2 (green) and RELN (red), respectively. (N) Immunostaining against CRB1 (green) highlights a subset of NPCE situated in proximity with neighboring ciliary processes. (O) RNA ISH for *MECOM* (green) highlights NPCE lining a ciliary process. Vasc_Endo, vascular endothelium; CM, ciliary muscle, CP, ciliary process; White scale bars: 100 μ m; yellow bars: 20 μ m.

were identified through their selective expression of melanocyte marker *PAX3*, as well as *EDNRB*, *MITF*, *MLANA*, *MLPH*, and *TYR* (Fig. 3 C and E). Smooth muscle cells comprising the iris sphincter muscle, responsible for constricting the pupil upon cholinergic stimulation, were identified by selective expression of the muscarinic receptor *CHRM3*, as well as *DES* (Fig. 3 C and D). The iris dilator muscle, responsible for dilating the pupil upon adrenergic stimulation, selectively expressed the alpha-1a adrenergic receptor *ADRA1A*. Both dilator and sphincter muscle cells expressed contractile genes, including *MYH11* and *ATP2A2* (Fig. 3C). The large, intensely pigmented cells of the PPE were visualized with immunostaining against RELN (Fig. 3G). Vascular endothelial cells, macrophages, lymphocytes, and Schwann cells were identified by expression of canonical markers (see above and ref. 23).

Ciliary Body. The CB consists of four main components: 1) ciliary muscle, responsible for accommodation and assistance in removal of aqueous humor; 2) stroma, the vascularized connective tissue core; 3) pigmented ciliary epithelium (PCE); and 4) nonpigmented ciliary epithelium (NPCE). The PCE and NPCE are single-layered epithelia that lie adjacent to each other, oriented apex-to-apex, and connected by gap junctions (Fig. 3H). Both play important roles in maintaining the blood-aqueous barrier and secreting aqueous humor.

Analysis of 34,132 CB single nucleus transcriptomes yielded 10 clusters (Fig. 3 I and J and *SI Appendix*, Fig. S1F). The most abundant corresponded to the PCE and NPCE. DE genes in the PCE included *ATP6V1C2*, encoding the H⁺ vacuolar ATPase; *SLC23A2*, encoding a sodium-dependent ascorbate transporter; and *SLC4A4*, encoding the sodium-bicarbonate cotransporter (NBC) (Fig. 3J). Other DE genes included *MAMDC1*, *CCBE1*, *DCT*, and numerous additional solute transporters (*SLC35G1*, *SLC38A11*, *SLC24A5*, *SLC9B2*, *SLC7A2*, and *SLC7A6*), consistent with the PCE's role alongside the NPCE in secreting aqueous humor. We visualized the PCE via immunostaining against RELN (Fig. 3M). DE genes that distinguished NPCE from PCE included the vitreous humor components, *COL9A1*, *COL9A3*, and *OPTC*, reflecting the NPCE's close association with this gel (28), as well as *ATPIA2*, *NECTIN3*, *CACNA1E*, *ENPP2*, and

the chloride transporter *BEST2*. The NPCE was visualized with immunostaining against LRP2, MECOM, and CRB1, with the latter being expressed by a subset of cells populating areas of the ciliary processes that were in contact with other processes (Fig. 3 M–O).

Cell types comprising the other clusters were determined by the expression of canonical markers. They included *DES* and *MYH11* for muscle, *DCN* and *PDPN* for fibroblasts (Fig. 3K), *LG14* and *SCN7A* for Schwann cells, *MLANA* for melanocytes (Fig. 3L), PECAM1 for vascular endothelium (Fig. 3K), *ADCY3* for pericytes, *CD163* for macrophages, and *CD96* for lymphocytes (Fig. 3J).

Lens. The lens occupies the space between the iris and the vitreous (Fig. 1A). It is suspended in position by the elastic zonular fibers running between the equatorial lens capsule and the ciliary processes (29) (Fig. 1B). The lens substance, composed of the central nucleus, concentrically layered cortical fibers, and lens epithelium, is enveloped by an elastic basement membrane called the lens capsule (Fig. 4A). Throughout life, lens epithelial cells that retain the capacity to divide migrate toward the post-equatorial region, where they terminally differentiate into cortical lens fiber cells (30, 31). Mature lens fiber cells lack most organelles, including the nucleus, ribosomes, and mitochondria, rendering them highly transparent.

Computational analysis divided 13,900 lens cell transcriptomes into 5 clusters (Fig. 4B and *SI Appendix*, Fig. S1E, and *Dataset S1*). Three were classified as lens epithelial cells due to their robust expression of the ocular epithelial marker *PAX6*. Their regional localizations as visualized by ISH for selectively expressed markers (*ATP8B4*, *CACNA1A1*, and *SLC1A2*) identified them as anterior, equatorial, and transitional types (Fig. 4 C–F, H, and I). Of note, cells in the transitional cluster expressed genes supporting differentiation into fiber cells (e.g., *JAG1*, *NAP1L4*, *BACH2*) (32–34). The remaining two clusters, visualized with ISH for *GPR160*, *CAV1*, and *UCHL1*, corresponded to nucleated fiber cells at different stages of maturity (Fig. 4 G–I).

The arrangement of these clusters mirrored the migratory and developmental trajectory of lens epithelial cells. Rather than being discrete, the clusters were continuous, describing a gradient leading

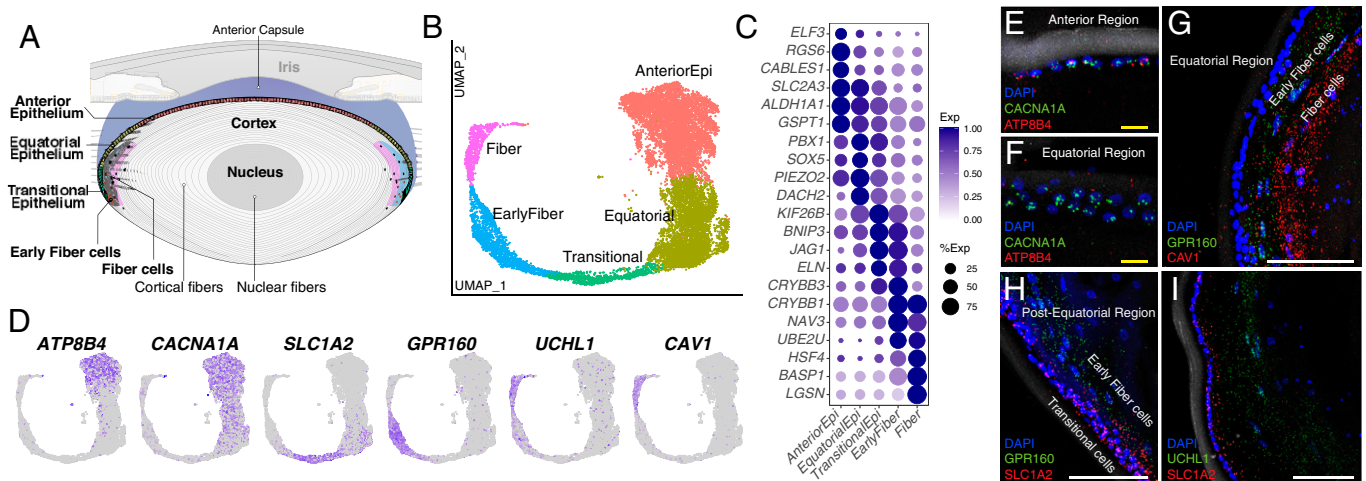


Fig. 4. Cells of the crystalline lens. (A) The human crystalline lens consists of lens epithelium and lens fiber cells. (B) Clustering of 13,900 single-nucleus expression profiles derived from lens tissue visualized by UMAP. A continuum is observed ranging from anterior epithelium to lens fiber cells. (C) Dot plot showing genes selectively expressed in cells of the lens. (D) Feature plots demonstrating DE genes corresponding to cells of the lens. (E and F) Lens epithelial cells visualized with ISH. Expression of *CACNA1A* (green) is evident in both anterior and equatorial epithelial cells, whereas *ATP8B4* (red) is confined to the anterior epithelium. (G) ISH demonstrates the expression of *GPR160* (green) by early lens fiber cells and *CAV1* (red) by more mature fiber cells. (H and I) Transitional lens epithelial cells in the post equatorial region are positive for *SLC1A2* (red) as visualized by ISH; early fiber cells are positive for *GPR160* (green); and fiber cells are positive for *UCHL1* (green). (White scale bars; 100 μ m; yellow bars; 20 μ m.)

from epithelial cell on one end of the spectrum to lens fiber cell on the other, as well as gradients of expression within each cluster (Fig. 4 C and D).

Scattered *TOP2A*⁺ cells were present in the lens epithelial clusters suggesting the capacity of a subset to proliferate, and a small group of cells was *PTPRC*⁺, suggestive of a resident immune population as recently described (35). Neither of these rare populations was large enough to generate a discrete cluster in our dataset.

Integrated Analysis. In several cases, cell types identified in one tissue resembled those in one or more other tissues. This observation raised the question of which cell types were present in multiple tissues and which were tissue specific. To address this issue, we pooled and reclustered data from iris, CB, cornea, CSW, and TM. The initial analysis indicated that cell types in the lens were distinct from those in the other structures, so they were omitted from this analysis. Altogether, integration yielded 34 clusters (Fig. 5A and *SI Appendix*, Figs. S5 A and B and S6A). A list of the DE genes from each type, as well as those from lens, is compiled in *Dataset S1*.

We tallied the origins of the cells within each cluster. In many cases, cells of a particular type were derived mostly or entirely from a single tissue—for example PCE cells from the CB, sphincter muscle from the iris, and goblet cells from the CSW (Fig. 5B and *SI Appendix*, Fig. S5B). In some cases, however, cells derived from multiple tissues coclustered. This was not surprising for immune cells, melanocytes, and Schwann cells but was unexpected for some other cell types.

Epithelium. Twelve clusters were identified as epithelial cells. Most were tissue specific, deriving primarily from iris, CB, CSW, or cornea/CSW, with the latter group presumably reflecting the presence of corneal tissue in the CSW (Fig. 5B). Based on transcriptomic similarity, they formed two clades. One comprised ocular surface types, and the other comprised uveal (iris and CB) types, consistent with their embryological origins from the surface ectoderm or the neuroectoderm of the optic cup, respectively (36). Transcriptional similarity further mirrored embryological origin among the four uveal epithelial types: the NPCE of the CB was transcriptionally more similar to the PPE of the iris, together representing the inner layer of the uveal bilayer (derived from the inner layer of the optic cup), and the PCE of the CB was more similar to the APE of the iris, together representing the outer layer of the uveal bilayer (derived from the outer layer of the optic cup) (Fig. 5B and E). Among ocular surface epithelial types, the limbal superficial and basal cell clusters were similar to their conjunctival counterparts and clustered together (i.e., “L_Conj_Epi-Superficial,” “L_Conj_Epi-Basal”).

Endothelium. Four clusters of vessel endothelial cells were identified through the expression of the canonical marker *PECAMI* (Fig. 5D). All four clusters were transcriptomic neighbors, and three were largely tissue specific (Fig. 5B). Two clusters corresponded to the vascular endothelium, likely reflecting different portions of the vascular tree. One of these, *CC_VenEndo*, was predominantly derived from the CSW tissue and expressed markers previously associated with collector channels and aqueous veins (*AQP1*, *POSTN*, *COL15A1*); it may also contain endothelium lining of other vessels of the venous tree, especially within scleral venous plexuses (23). The other, *Vasc_Endo*, was present in multiple tissues and may correspond to capillary endothelium and/or endothelium lining vessels of the arterial tree (37). Two other clusters corresponded to the lymphatic endothelium (*PDPN*⁺, *PKHD1L1*⁺, *SI Appendix*, Fig. S6H), predominantly localized to the conjunctival subepithelial

stroma, and to the Schlemm canal endothelium (*FNI*⁺ *PLAT*⁺, Fig. 5 D and K). The predominantly TM source of this latter cluster supports the notion that the Schlemm canal endothelium is a unique endothelium specialized for the conventional outflow path. Immunostaining against *PKHD1L1* highlighted closely related conjunctival lymphatics and Schlemm canal endothelia (Fig. 5L) but not blood vessels.

Pericytes. Two distinct pericyte clusters were identified by the shared expression of *PDGFRB*, *ADCY3*, *JAG1*, and *NOTCH3* (Fig. 5F). Pericyte1 (*LAMA2*⁺, *TRPC4*⁺) was derived mostly from TM and CB, whereas Pericyte2 (*ID4*⁺, *TRPC6*⁺, *RGS6*⁺) was derived almost exclusively from the CSW (Fig. 5B and *SI Appendix*, Fig. S6 A and I–L).

Fibroblasts. Six transcriptomically related clusters expressed genes diagnostic of fibroblasts (e.g., *PDGFRA*, *COL6A3*, *DCN*, *PRRX1*, *CDH11*; Fig. 5 B and C). Five were assigned based on tissue source and histological validation: TM fibroblasts derived from tissue within the TM and CSW dissections; iris fibroblasts derived predominantly from the iris; ciliary fibroblasts derived primarily from the ciliary muscle tissue within the TM, CSW, and CB (annotated as “uveal fibroblasts” in the TM/CSW atlas, above); corneal fibroblasts, derived predominantly from cornea and corneal component of the CSW dissection; and scleral fibroblasts derived exclusively from the scleral and/or limbal component of the CSW dissection. The sixth cluster, *FibroX*, from limbus, remains uncharacterized.

Three of the fibroblast clusters—iris, ciliary, and TM fibroblasts—were closely related and shared numerous markers (e.g., *MYOC*, *PDPN*, and *RSPO2*). However, each expressed distinct markers as follows that enabled histological validation to support their predominant tissue source: *WIF1* and *ETNPPL* for iris fibroblasts; *BMP5*, *PII6*, and *C7* for ciliary fibroblasts; and *NEB*, *NELL2*, *UNC5D*, and *TMEM178A* for TM fibroblasts (Fig. 5 I and J and *SI Appendix*, Figs. S4 E and F and S6 C–F). In addition, a subset of cells from each one of these clusters was derived from the TM tissue dissection (Fig. 5B) and shared DE genes with TM cell types previously described and validated as “BeamA,” “BeamB,” and “JCT” in a previous scRNAseq study (23). For example, markers of Beam A (e.g., *BMP5*) were expressed predominantly by the ciliary fibroblast cluster representing cells populating the ciliary muscle and uveal base of the TM; markers of Beam B (*TMEFF2*) and JCT (*CHI3L1*) were expressed by largely nonoverlapping populations within the iris and TM fibroblast clusters, respectively, and exhibited correspondingly nonoverlapping staining within the iridocorneal angle on histology (*SI Appendix*, Figs. S4 E–G and S6B). In a contemporaneous scRNAseq study of the TM with largely consistent results (25), DE markers of TM1 overlapped with the ciliary fibroblast cluster and those of TM2 overlapped with the current TM fibroblast cluster. We envision two possible explanations for the difference between the current and previous studies (23, 25). One is that some cells in the TM dissections may have been derived from neighboring tissues—a complication that only became apparent when we profiled those tissues separately. We favor the alternative, that the similarity is genuine, which would be consistent with the TM being populated to varying degrees by three subsets of neural-crest-derived mesenchymal cells derived by migration from the contiguous iris and CB. In this view, the three clusters may be considered “outflow fibroblasts,” populating a key area within the iridocorneal angle where aqueous drains through the conventional or uveoscleral pathway.

Melanocytes. In the CSW atlas described earlier, two types of melanocytes were identified, namely, conjunctival and uveal, with the latter deriving from the ciliary muscle component of

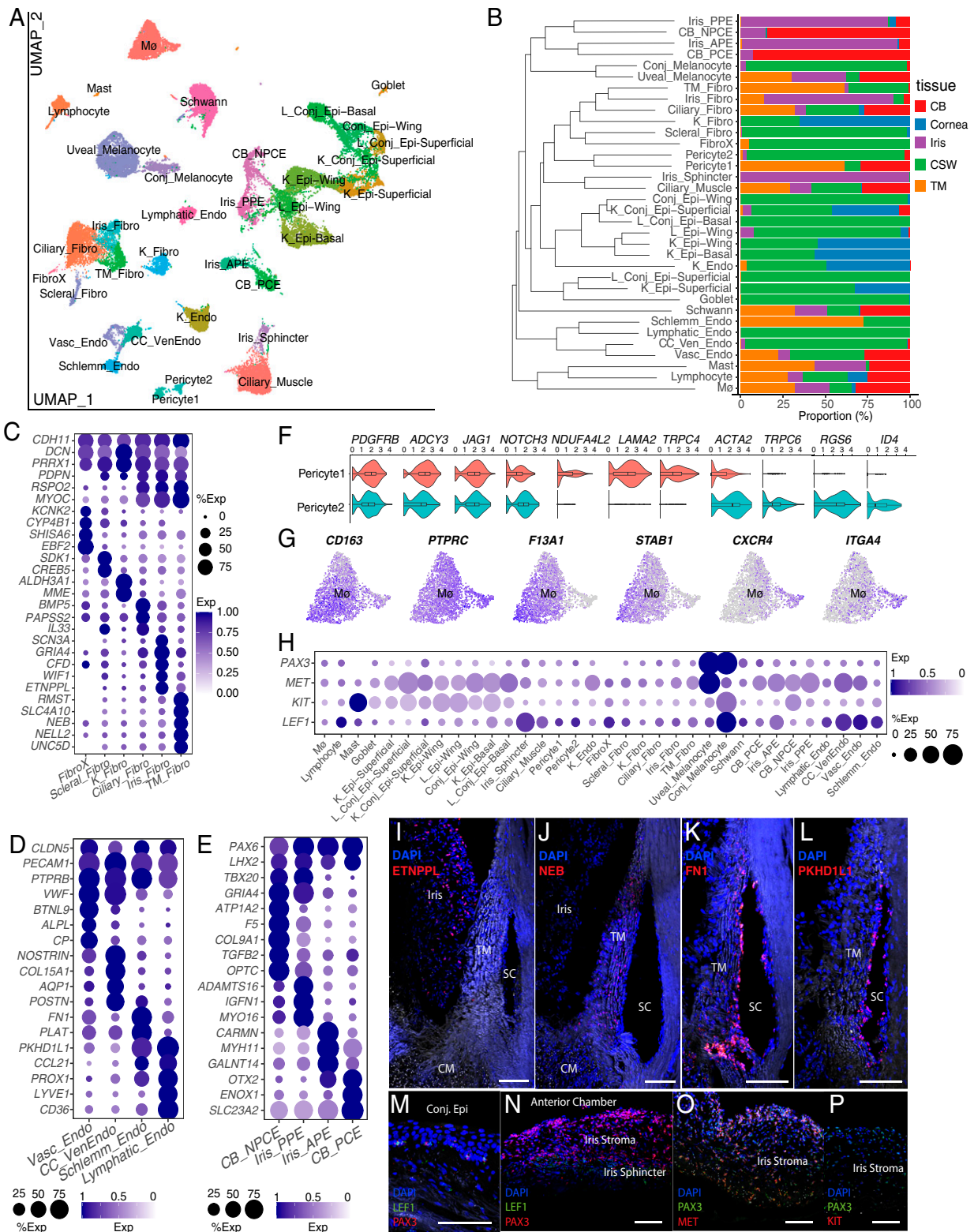


Fig. 5. Integrated analysis of cells populating the human anterior segment. (A) Clustering of expression profiles pooled for the integrated analysis and visualized by UMAP. (B) Stacked bar chart indicating proportions within each cluster contributed by separate tissue sources. Transcriptional relatedness indicated by dendrogram. (C–E) Dot plot showing common and DE genes in fibroblast types (C), vessel endothelial types (D), and uveal epithelium. (F) Violin plots showing common and selectively expressed genes in the two pericyte clusters. Here and in other violin plots, the scale on y axis represents expression level, calculated as a normalized $\log(\text{UMI}+1)$ value. (G) Feature plots demonstrating expression patterns within the macrophage cluster. (H) Dot plot showing cell-type-specific expression of *PAX3*, *MET*, *KIT*, and *LEF1*. (I) Iris fibroblasts selectively expressing *ETNPPL* (red), visualized with RNA ISH. (J) TM fibroblasts selectively expressing *NEB* (red), visualized with RNA ISH. (K) Schlemm canal (SC) endothelium expressing *FN1* (red), visualized with RNA ISH. (L) SC endothelium expressing *PKHD1L1* (red), visualized with RNA ISH. (M) Melanocytes within the basal layer of the conjunctiva visualized with ISH for *PAX3* (red) and *LEF1* (green). Consistent with expression pattern seen in H, vascular endothelium lining a vessel within the conjunctival stroma is also noted to be positive for *LEF1* (green). (N) Melanocytes within the iris stroma, visualized with RNA ISH for *PAX3* (red), do not express *LEF1* (green, absent). The iris sphincter is instead positive for *LEF1*, consistent with expression noted in H. (O) Uveal melanocytes within the iris anterior border layer and stroma visualized with ISH for *MET* (red) and *PAX3* (green). (P) Melanocytes within the iris stroma, visualized with ISH for *PAX3* (red), do not express *KIT* (green, absent). L, Limbus; Conj Epi, conjunctival epithelium. Remaining abbreviations as in previous figures. (White scale bars: 100 μm .)

the CSW dissection. An integrated analysis supported this distinction; melanocytes derived from the iris and CB coclustered with the uveal melanocytes (*MET+*) identified in the CSW, and these cells remained distinct from the conjunctival melanocytes (*KIT+* and *LEF1+*) (Fig. 5 *M–P* and *SI Appendix, Fig. S5C*).

Macrophages. Although all macrophages grouped together in a single cluster regardless of tissue source, a closer inspection indicated substantial heterogeneity. Macrophages of corneal origin were too few in number to form a distinct cluster but segregated within a discrete zone, demonstrating the expression of *CXCR4* and *ITGA4* but not *LYVE1* or *F13A1*. In contrast, the remainder of the macrophage cluster, which derived from the other tissues, expressed *LYVE1*, *STAB1*, and *F13A1* (Fig. 5 *G* and *SI Appendix, Fig. S5D*). Although immune cell heterogeneity in particular must be interpreted with caution in a small postmortem donor pool, all donors contributed similarly to the macrophage population, and the distribution of subpopulations was similar across all donors.

Disease Associations. Many genes have been implicated in susceptibility to ocular diseases that result from defects in the anterior segment. We explored expression patterns of 924 disease-associated genes to the cell types in our atlas.

Mendelian Genes.

Anterior segment dysgenesis (ASD). Congenital and developmental abnormalities of the anterior segment can affect the iris, iridocorneal angle drainage structures, and cornea (38). Due to dysregulated aqueous outflow, ~50% of patients with ASD develop glaucoma (39). Genes implicated in ASD and glaucoma include *PAX6*, *PITX2*, *FOXC1*, *CYP1B1*, *LTBP2*, *FOXE3*, *PITX3*, *B3GLCT*, *COL4A1*, *PXDN*, and *CPAMD8*. Many of these genes, which play well-defined roles in ocular development, continue to be expressed in relevant adult cell types within the anterior segment (Fig. 6 *A* and *B* and *SI Appendix, Fig. S7A*).

Glaucoma. Glaucoma is a phenotypically heterogeneous disease with a final common outcome of optic nerve degeneration, with elevated IOP representing the only known modifiable risk factor (40). We explored expression patterns of Mendelian genes associated with glaucoma (including ASD-related glaucoma) and elevated IOP, including *MYOC*, *ANGPT1*, *ANGPT2*, and *LMX1B* as well as *PITX2*, *FOXC1*, *LTBP2*, and *CPAMD8*. As expected, most of them were robustly expressed in outflow pathway cells and other glaucoma-relevant cell types (Fig. 6 *A* and *SI Appendix, Fig. S7*).

Cataract. Defined as opacity in the crystalline lens, cataract is the leading cause of blindness worldwide and generally follows a bimodal age distribution corresponding to congenital and age-related onset. Hereditary congenital cataracts, presenting at birth or during infancy, have been associated with highly penetrant genetic mutations in lens crystallins, growth factors, transcription factors, connexins, intermediate filament proteins, membrane proteins, the protein degradation apparatus, and a variety of other pathways including lipid metabolism (41). Crystallin genes were strongly expressed across lens epithelial and fiber cell types with gradient differences for a subset of genes. For example, *CRYAB*, *CRYGS*, and *CRYBB2* were broadly expressed across all lens clusters (spanning both epithelial and fiber cell types), whereas *CRYBB3* and *CRYBA1* were most prominently expressed in transitional epithelium and early fiber cells and *CRYBA4*, *CRYGD*, and *CRYBB1* were enriched in lens fibers (Fig. 6 *B*). The connexin gene *GJA3* demonstrated a similar expression pattern beginning in transitional epithelium and extending variably

into the fiber cells. Among other associated congenital cataract genes, we noted peak expression either in the early fiber cells (e.g., *LIM2*, *TDRD7*) or the more mature fiber cells (e.g., *BFSP1*, *BFSP2*, *TMEM114*, *HSF4*). Only a minority of cataract-associated genes demonstrated predominant expression in the lens epithelial (as opposed to fiber cell) clusters, and most of them were in the setting of pleomorphic syndromes (*PAX6*, *RGS6*, *TSPAN12*).

Corneal dystrophies. The corneal dystrophies are inherited conditions that impair the transparency of the cornea, leading to reduced vision and in some cases chronic ocular pain (42). Although these conditions have variable presentations, many have clinical findings predominantly localized within one of the three major layers of the cornea. We found a tight correspondence between cell-type-specific expression and the predominant clinical finding. Genes implicated in epithelial corneal dystrophies, including *KRT3* and *KRT12* (Meesman) and *COL17A1* (recurrent erosion), were expressed predominantly in the wing and basal cells of the corneal epithelium (Fig. 2 *C* and *SI Appendix, Fig. S2A*). Genes implicated in endothelial dystrophies, including *COL8A2* (Posterior polymorphous) and *SLC4A11* (Congenital Hereditary type 2), were expressed predominantly in the corneal endothelium (Fig. 6 *C*). Finally, genes implicated in stromal dystrophies, including *CHST6* (macular), *DCN* (congenital stromal), and *TGFBI* (lattice and granular), were expressed in keratocytes, with the latter also expressed in the epithelium (Fig. 6 *C*).

Ectopia lentis.

Ectopia lentis (EL) is a condition in which the crystalline lens is abnormally positioned within the eye, most often due to damaged, dysfunctional, or absent zonular fibers (43, 29). The most common cause of EL is trauma, but mutations have been implicated in both isolated cases (e.g., *ADAMTSL4*) and in syndromes such as Marfan syndrome (*FBN1*), Weill Marchesani syndrome (*ADAMTSL0*, *ADAMTSL17*) Knobloch syndrome (*COL18A1*), aniridia (*PAX6*), and homocystinuria (*CBS*, *MTR*, *MTHFR*). EL-associated genes were consistently expressed in the nonpigmented ciliary epithelial and/or the equatorial and transitional lens epithelial cells, which are located in areas adjacent to zonules, suggesting that they contribute to ongoing structural integrity of this important apparatus (Fig. 6 *B*). *LOXLI*, implicated in pseudo-foliation syndrome—a condition in which zonular fibers become brittle over time—was also expressed most prominently in the equatorial lens epithelium (Fig. 6 *B*).

Susceptibility Genes Nominated by GWAS Analysis. Susceptibility to common ocular conditions such as myopia, age-related cataract, and primary open angle glaucoma (POAG) is conferred by multiple common genetic variants with small effect sizes, many of which have been identified by genome-wide association study (GWAS). In addition to interrogating each gene individually (*SI Appendix, Fig. S8 A–H*), we developed a gene expression score (*Materials and Methods*) to explore whether GWAS-identified genes associated with these complex traits were more likely to be expressed in specific subsets of cell types. Because both the anterior and posterior segments are involved in POAG and myopia, we applied this analysis to key retinal cell types, alongside the anterior segment atlas (Fig. 6 *D* and *SI Appendix, Fig. S7B*). Patterns were broadly consistent with our current knowledge of disease mechanisms. Genes associated with cataract were enriched in lens cell types. Genes associated with POAG were most enriched in TM cells, cell types of outflow tissues within the iridocorneal angle (ciliary and iris fibroblasts), and corneal endothelium (e.g., *POU6F2*, associated with thin central corneal thickness, a highly heritable trait and independent risk factor for development of POAG) (44). Moderate

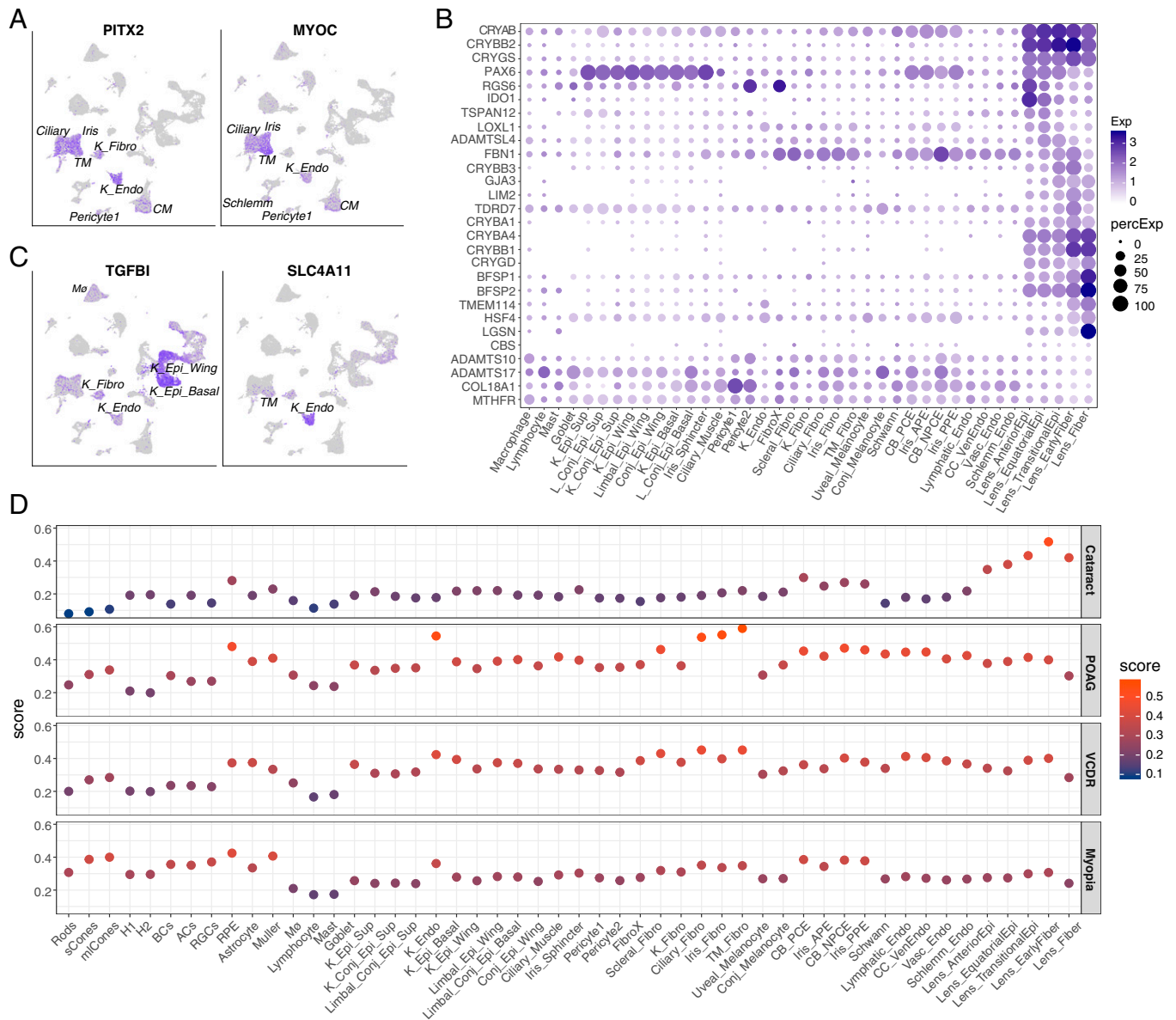


Fig. 6. Expression of ocular disease-associated genes. (A) Feature plots demonstrating enriched expression of glaucoma-associated genes within cell types localized to the iridocorneal angle drainage structures. (B) Dot plot showing cataract- and EL-associated genes. (C) Feature plot showing expression patterns of genes implicated in corneal dystrophies. (D) Dot plot showing cell-type-specific enrichment scores of genes identified through GWAS for common conditions or traits. Major retinal cell types from normal macula are also included. Cell type abbreviations are as in previous figures. H1/H2, horizontal cells; BC, bipolar cells; AC, amacrine cells; RGC, retinal ganglion cells.

enrichment scores in retinal pigment epithelium (RPE), Muller glia, scleral fibroblasts, CB epithelium, and vessel endothelium are consistent with the disease's complex pathophysiology and potential diversity of phenotypes. Genes associated with vertical cup-to-disk ratio (VCDR) demonstrated similar enrichment patterns to POAG, albeit they were less pronounced. Finally, myopia-associated genes were most strongly enriched in cells of the neural retina (specifically retinal ganglion cells, RPEs, and cones), as well as uveal epithelium and corneal endothelium.

Discussion

We used snRNAseq to profile cells comprising the human anterior segment, generating discrete cell atlases of the cornea, limbus, iris, CB, and lens. We then merged these datasets to perform an integrated analysis that enabled holistic appraisal of these cells across contiguous and interdependent ocular tissues. Finally, we used the atlases to interrogate cell-type-specific

expression patterns of disease-associated genes, gleaning insights into where they act.

Tissue-Specific and Shared Cell Types. Our analysis of anterior segment structures defined many clusters, each presumably belonging to a single cell type or a small number of closely related types that were too transcriptomically similar to separate in the current dataset. Adding these results to those from our recent analysis of the TM and contiguous structures (23) but taking shared types from the integrated analysis into account, we estimate that there are at least 40 cell types in the human anterior segment. Our results are generally concordant with those of a recent whole eye atlas (45), but the larger number of anterior segment cells in our dataset than theirs (195,248 vs. <30,000) allowed us to document far more cell types.23

It was apparent that some of the types isolated from a particular tissue were very similar to ones isolated from other tissues. This is unsurprising for three reasons. First, although the structures we

analyzed can be roughly separated by dissection, some are contiguous without sharply defined borders. For example, the iris root, TM, and ciliary muscle share a common insertion area at the iridocorneal angle (Fig. 1*B*) and limbus is continuous with the cornea and sclera (Fig. 2*A*) such that discrete anatomical dissection at the cellular level is impossible. Second, some of the major cell types, such as macrophages, are motile and can easily cross tissue boundaries. Third, some types, such as melanocytes, Schwann cells, and outflow fibroblasts populating the iridocorneal angle, are derived from the neural crest, a migratory population that invades multiple structures during development (46).

By combining transcriptomes from contiguous tissues, reclustered them, and visualizing key markers with histological methods, we were able to determine which types are shared and which are primarily confined to specific tissues. Most epithelial types were tissue specific whereas immune cells (mast cells, macrophages, and lymphocytes) and Schwann cells (crest derived) were shared. For other groups, distribution was more complex. For pericytes, melanocytes, and endothelia, one type populated multiple tissues, whereas the other (or others for endothelia) was tissue specific. Of particular interest were the melanocytes, with a conjunctival type derived from the CSW on the surface of the eye and a uveal type inside the eye present in multiple structures. The substantial differences between their transcriptomes may carry important implications in disease research. Uveal melanoma and conjunctival melanoma—representing serious oncologic diagnoses—behave very differently in the clinical setting and consequently require different treatment approaches (47); their distinct molecular features may provide insight into pathogenesis and therapeutic strategies.

Additional insights were gleaned for fibroblasts. Despite representing a diverse group of cells that play a key role in maintaining health and driving disease, fibroblasts throughout the body have historically been poorly characterized. Single-cell technologies have contributed significantly to advancing our understanding of their heterogeneity and contributions to disease states (27). Our current work extends this analysis to fibroblasts within the anterior segment of the eye, particularly those populating the TM. Indeed, only by examining the TM together with surrounding contiguous tissues were we able to appreciate both its relatedness to the cornea, CB, and iris as well as its unique aspects. Among the anterior segment fibroblast cells, we found the TM cells to be most closely related to fibroblasts residing in the CB and iris tissues. In contrast, fibroblasts from the cornea and sclera were distinctly different, with each defined by a unique set of ECM and collagen genes.

A prominent illustration of tissue-specific cell types exhibiting relationships corresponding to their contiguity and embryological origins involved the cells populating the uveal epithelial bilayer lining the iris and CB, whose origins trace to the neuroectodermal bilayer of the optic cup (48). The iris PPE demonstrated the closest transcriptomic relation to the nonpigmented CB NPCE, together comprising the inner layer of the uveal epithelial bilayer derived from the inner layer of the embryological optic cup. Similarly, the iris APE demonstrated the closest relation to the pigmented CB PCE, together comprising the outer layer of the uveal epithelial bilayer derived from the outer layer of the embryological optic cup. Although we did not integrate posterior segment tissues into our analysis, we speculate that the RPE may show similarity to the other two cell types in this outer uveal epithelial layer. Similarly, the embryological origin of the neural retina links it to the inner uveal layer, which may account for some residual neural-type expression patterns in the CB nonpigmented epithelium and the iris PPE (e.g., *CRB1*, *LRRN2*, *CACNA1E*).

A caveat to the classification system is that we defined clusters or types using clustering algorithms that, while nominally

unsupervised, depend on the parameters we choose. This is especially relevant in cases where gene expression differences occur on a continuum among cells. For example, in several instances, we noted that the expression of specific genes displayed gradients within a cluster, suggesting the existence of either additional closely related cell types or cell-state-related patterns of expression. Conversely, given the limited numbers of cells used, there may be tissue-specific differences among nominally shared types that we were unable to detect.

Disease-Associated Genes. Our cell atlas of the human anterior segment provides a valuable resource for analyzing genes implicated in ocular disease. Several results were noteworthy. For example, it expands our insight into the complexity of glaucoma, where outflow fibroblasts (including those populating the TM, CB, and iris), corneal endothelium, and vessel endothelia (including those populating Schlemm canal, lymphatic, and blood vessels) emerged as key cell types expressing genes associated with POAG and IOP. In cataract, transitional lens epithelium and early fiber cells express the majority of disease-associated genes. In myopia, the uveal epithelium, RPE, and various neural cell types in the retina appeared to stand out as important expressors of associated genes.

Materials and Methods

Tissue Acquisition, Dissection, and Processing. Human ocular tissues were obtained postmortem either from Massachusetts General Hospital (MGH) via the Rapid Autopsy Program or from The Lion's Eye Bank in Murray, Utah. The acquisition and use of human tissue were approved by the Human Study Subject Committees (Dana Farber/Harvard Cancer Center Protocol No. 13-416, University of Utah Protocol IRB_00010201) (*SI Appendix, Tables S1 and S2*). Human tissue used for immunohistochemistry (IHC) was also provided by the Lions Vision Gift, Portland, OR. No ocular disease was reported in any of the human donors, and no abnormalities were noted during dissection. Single nuclei libraries were generated, sequenced, and analyzed by methods similar to those in van Zyl et al. (23) with modifications detailed in *SI Appendix, Methods*.

Histology. CSWs or whole globes were fixed, frozen, and sectioned in a cryostat. Sections were processed for IHC or ISH. Antibodies and probes used are listed in *SI Appendix, Table S3*. Images were acquired on Zeiss LSM 710 confocal microscopes and analyzed using ImageJ (NIH).

Data Availability. The accession number at Gene Expression Omnibus for the raw data reported in this paper is [GSE199013](https://www.ncbi.nlm.nih.gov/geo/query/acc.cgi?acc=GSE199013) (49). Data can also be visualized in the Broad Institute's Single Cell Portal (50).

ACKNOWLEDGMENTS. This work was supported by grants from the NIH (5K12EY016335, EY028633, and U01 MH105960); the Chan-Zuckerberg Initiative (CZF-2019-002459); the Klarman Cell Observatory of the Broad Institute of MIT and Harvard; an unrestricted grant from Research to Prevent Blindness to the Department of Ophthalmology and Visual Sciences, University of Utah; and by charitable donations to the Sharon Eccles Steele Center for Translational Medicine. We thank Chris Pappas and Lisa Nichols for their efforts to acquire and process ocular tissues, Maria Diaz de la Loza for the superb illustrations, and the tissue donors and their families for their generosity.

Author affiliations: ^aDepartment of Ophthalmology, Harvard Medical School, Boston, MA 02115; ^bCenter for Brain Science, Harvard University, Cambridge, MA 02138; ^cDepartment of Molecular and Cellular Biology, Harvard University, Cambridge, MA 02138; ^dBoston Children's Hospital, F.M. Kirby Neurobiology Center, Boston, MA 02115; ^eSharon Eccles Steele Center for Translational Medicine, John A. Moran Eye Center, University of Utah, Salt Lake City, UT 84132; and ^fDepartment of Ophthalmology and Visual Sciences, University of Utah, Salt Lake City, UT 84132

Author contributions: T.v.Z., W.Y., and J.R.S. designed research; T.v.Z., A.M.M., and A.M. performed research; G.S.H. contributed new reagents/analytic tools; T.v.Z., W.Y., and A.M. analyzed data; and T.v.Z. and J.R.S. wrote the paper.

Reviewers: S.B., Washington University in St. Louis School of Medicine; R.L., Northwestern University; and J.S., New York University.

1. J. D. Adelson *et al.*, Causes of blindness and vision impairment in 2020 and trends over 30 years, and prevalence of avoidable blindness in relation to VISION 2020: The Right to Sight: An analysis for the Global Burden of Disease Study. *Lancet Glob. Health* **9**, e144–e160 (2020).
2. G. X. Zheng *et al.*, Massively parallel digital transcriptional profiling of single cells. *Nat. Commun.* **8**, 14049 (2017).
3. D. W. DelMonte, T. Kim, Anatomy and physiology of the cornea. *J. Cataract Refract. Surg.* **37**, 588–598 (2011).
4. A. C. Mita, M. M. Mita, S. T. Nawrocki, F. J. Giles, Survivin: Key regulator of mitosis and apoptosis and novel target for cancer therapeutics. *Clin. Cancer Res.* **14**, 5000–5005 (2008).
5. F. M. Townsley, A. Aristarkhov, S. Beck, A. Hershko, J. V. Ruderman, Dominant-negative cyclin-selective ubiquitin carrier protein E2-C/UbcH10 blocks cells in metaphase. *Proc. Natl. Acad. Sci. U.S.A.* **94**, 2362–2367 (1997).
6. J. L. Nitiss, DNA topoisomerase II and its growing repertoire of biological functions. *Nat. Rev. Cancer* **9**, 327–337 (2009).
7. J. M. Li *et al.*, Single-cell transcriptomics identifies a unique entity and signature markers of transit-amplifying cells in human corneal limbus. *Invest. Ophthalmol. Vis. Sci.* **62**, 36 (2021).
8. P. Català *et al.*, Single cell transcriptomics reveals the heterogeneity of the human cornea to identify novel markers of the limbus and stroma. *Sci. Rep.* **11**, 21727 (2021).
9. E. M. Van Buskirk, The anatomy of the limbus. *Eye (Lond.)* **3**, 101–108 (1989).
10. C. Bonnet *et al.*, Human limbal epithelial stem cell regulation, bioengineering and function. *Prog. Retin. Eye Res.* **85**, 100956 (2021).
11. A. G. Seyed-Safi, J. T. Daniels, The limbus: Structure and function. *Exp. Eye Res.* **197**, 108074 (2020).
12. R. M. Lavker, N. Kaplan, J. Wang, H. Peng, Corneal epithelial biology: Lessons stemming from old to new. *Exp. Eye Res.* **198**, 108094 (2020).
13. A. Ramirez-Miranda, M. N. Nakatsu, S. Zarei-Ghanavati, C. V. Nguyen, S. X. Deng, Keratin 13 is a more specific marker of conjunctival epithelium than keratin 19. *Mol. Vis.* **17**, 1652–1661 (2011).
14. S. Yoshida *et al.*, Cytokeratin 15 can be used to identify the limbal phenotype in normal and diseased ocular surfaces. *Invest. Ophthalmol. Vis. Sci.* **47**, 4780–4786 (2006).
15. S. Merjavia, A. Neuwirth, M. Tanzerova, K. Jirsova, The spectrum of cytokeratins expressed in the adult human cornea, limbus and perilimbal conjunctiva. *Histol. Histopathol.* **26**, 323–331 (2011).
16. Y. W. Wong, J. Chew, H. Yang, D. T. H. Tan, R. Beuerman, Expression of insulin-like growth factor binding protein-3 in pterygium tissue. *Br. J. Ophthalmol.* **90**, 769–772 (2006).
17. H. C. Turner, M. T. Budak, M. A. M. Akinci, J. M. Wolosin, Comparative analysis of human conjunctival and corneal epithelial gene expression with oligonucleotide microarrays. *Invest. Ophthalmol. Vis. Sci.* **48**, 2050–2061 (2007).
18. D. L. Shurman, L. Glazewski, A. Gumpert, J. D. Zieske, G. Richard, In vivo and in vitro expression of connexins in the human corneal epithelium. *Invest. Ophthalmol. Vis. Sci.* **46**, 1957–1965 (2005).
19. J. Collin *et al.*, A single cell atlas of human cornea that defines its development, limbal progenitor cells and their interactions with the immune cells. *Ocul. Surf.* **21**, 279–298 (2021).
20. A. J. Ligocki *et al.*, Molecular characteristics and spatial distribution of adult human corneal cell subtypes. *Sci. Rep.* **11**, 16323 (2021).
21. D. Q. Li *et al.*, Single-cell transcriptomics identifies limbal stem cell population and cell types mapping its differentiation trajectory in limbal basal epithelium of human cornea. *Ocul. Surf.* **20**, 20–32 (2021).
22. S. Dou *et al.*, Molecular identity of human limbal heterogeneity involved in corneal homeostasis and privilege. *Ocul. Surf.* **21**, 206–220 (2021).
23. T. van Zyl *et al.*, Cell atlas of aqueous humor outflow pathways in eyes of humans and four model species provides insight into glaucoma pathogenesis. *Proc. Natl. Acad. Sci. U.S.A.* **117**, 10339–10349 (2020).
24. I. K. Gipson, Goblet cells of the conjunctiva: A review of recent findings. *Prog. Retin. Eye Res.* **54**, 49–63 (2016).
25. G. Patel *et al.*, Molecular taxonomy of human ocular outflow tissues defined by single-cell transcriptomics. *Proc. Natl. Acad. Sci. U.S.A.* **117**, 12856–12867 (2020).
26. W. D. Stamer, A. F. Clark, The many faces of the trabecular meshwork cell. *Exp. Eye Res.* **158**, 112–123 (2017).
27. M. B. Buechler *et al.*, Cross-tissue organization of the fibroblast lineage. *Nature* **593**, 575–579 (2021).
28. M. M. Le Goff, P. N. Bishop, Adult vitreous structure and postnatal changes. *Eye (Lond.)* **22**, 1214–1222 (2008).
29. S. Bassnett, Zinn's zonule. *Prog. Retin. Eye Res.* **82**, 100902 (2021).
30. S. Bassnett, H. Šikić, The lens growth process. *Prog. Retin. Eye Res.* **60**, 181–200 (2017).
31. T. Mochizuki, I. Masai, The lens equator: A platform for molecular machinery that regulates the switch from cell proliferation to differentiation in the vertebrate lens. *Dev. Growth Differ.* **56**, 387–401 (2014).
32. T. T. Le, K. W. Conley, N. L. Brown, Jagged 1 is necessary for normal mouse lens formation. *Dev. Biol.* **328**, 118–126 (2009).
33. T. Tanaka, Y. Hozumi, A. M. Martelli, M. Iino, K. Goto, Nucleosome assembly proteins NAP1L1 and NAP1L4 modulate p53 acetylation to regulate cell fate. *Biochim. Biophys. Acta Mol. Cell Res.* **1866**, 118560 (2019).
34. Y. Zhao, D. Zheng, A. Cvekl, A comprehensive spatial-temporal transcriptomic analysis of differentiating nascent mouse lens epithelial and fiber cells. *Exp. Eye Res.* **175**, 56–72 (2018).
35. A. S. Menko *et al.*, Resident immune cells of the avascular lens: Mediators of the injury and fibrotic response of the lens. *FASEB J.* **35**, e21341 (2021).
36. A. Cvekl, E. R. Tamm, Anterior eye development and ocular mesenchyme: New insights from mouse models and human diseases. *BioEssays* **26**, 374–386 (2004).
37. J. C. Schupp *et al.*, Integrated single-cell atlas of endothelial cells of the human lung. *Circulation* **144**, 286–302 (2021).
38. A. S. Ma, J. R. Grigg, R. V. Jamieson, Phenotype-genotype correlations and emerging pathways in ocular anterior segment dysgenesis. *Hum. Genet.* **138**, 899–915 (2019).
39. W. L. Alward, Axenfeld-Rieger syndrome in the age of molecular genetics. *Am. J. Ophthalmol.* **130**, 107–115 (2000).
40. J. D. Stein, A. P. Khawaja, J. S. Weizer, Glaucoma in adults—screening, diagnosis, and management: A review. *JAMA* **325**, 164–174 (2021).
41. A. Shiels, J. F. Hejtmancik, Mutations and mechanisms in congenital and age-related cataracts. *Exp. Eye Res.* **156**, 95–102 (2017).
42. W. Lisch, J. S. Weisz, Early and late clinical landmarks of corneal dystrophies. *Exp. Eye Res.* **198**, 108139 (2020).
43. A. Chandra, D. Charteris, Molecular pathogenesis and management strategies of ectopia lentis. *Eye (Lond.)* **28**, 162–168 (2014).
44. R. King *et al.*; International Glaucoma Genetics Consortium; NEIGHBORHOOD Consortium, Genomic locus modulating corneal thickness in the mouse identifies POU6F2 as a potential risk of developing glaucoma. *PLoS Genet.* **14**, e1007145 (2018).
45. P. Gautam *et al.*, Multi-species single-cell transcriptomic analysis of ocular compartment regulons. *Nat. Commun.* **12**, 5675 (2021).
46. J. Wang, A. Rattner, J. Nathans, A transcriptome atlas of the mouse iris at single-cell resolution defines cell types and the genomic response to pupil dilation. *eLife* **10**, e73477 (2021).
47. J. W. Harbour, Uveal and conjunctival melanoma: Close together—But only distantly related. *Oncology (Williston Park)* **30**, 44, 48 (2016).
48. S. Fuhrmann, Eye morphogenesis and patterning of the optic vesicle. *Curr. Top. Dev. Biol.* **93**, 61–84 (2010).
49. van Zyl *et al.*, Cell atlas of the human ocular anterior segment: Tissue-specific and shared cell types. Gene Expression Omnibus. <https://www.ncbi.nlm.nih.gov/geo/query/acc.cgi?acc=GSE1199013>. Deposited 20 March 2022.
50. van Zyl *et al.*, Cell atlas of the human ocular anterior segment: Tissue-specific and shared cell types. Broad Single Cell Portal. https://singlecell.broadinstitute.org/single_cell/study/SCP1841. Deposited 20 March 2022.